Observation of Nonreciprocal Wave Propagation in a Dynamic Phononic Lattice

Yifan Wang,[1,*] Behrooz Yousefzadeh,[1,*] Hui Chen,[2] Hussein Nassar,[2] Guoliang Huang,[2] and Chiara Daraio[1]
[1]Division of Engineering and Applied Science, California Institute of Technology, Pasadena, California 91125, USA
[2]Department of Mechanical and Aerospace Engineering, University of Missouri, Columbia, Missouri 65211, USA

(Received 23 April 2018; published 9 November 2018)

Acoustic waves in a linear time-invariant medium are generally reciprocal; however, reciprocity can break down in a time-variant system. In this Letter, we report on an experimental demonstration of nonreciprocity in a dynamic one-dimensional phononic crystal, where the local elastic properties are dependent on time. The system consists of an array of repelling magnets, and the on-site elastic potentials of the constitutive elements are modulated by an array of electromagnets. The modulation in time breaks time-reversal symmetry and opens a directional band gap in the dispersion relation. As shown by experimental and numerical results, nonreciprocal mechanical systems like the one presented here offer opportunities to create phononic diodes that can serve for rectification applications.

DOI: 10.1103/PhysRevLett.121.194301

Phononic crystals and metamaterials control acoustic waves through the geometry of their building blocks, engineered with periodic impedance mismatches and/or local resonances [1–7]. The majority of current realizations focuses on designing metamaterials in their spatial dimensions, while the material properties remain unchanged over time. This design framework restricts the application of metamaterials in scenarios where a material's tunability and adaptivity are required [8,9]. More importantly, in these time-invariant metamaterials, reciprocity holds as a fundamental principle in wave propagation, requiring the transmission of information or energy between any two points in space to be symmetric for opposite propagating directions [10].

However, nonreciprocal materials or devices, i.e., diodes, are usually required for rectification and control of the associated energy flow. Unlike electric diodes, mechanical or acoustic diodes are just starting to be explored [11–18]. Achieveing nonreciprocity in mechanical systems through intrinsic time-reversal symmetry breaking has been demonstrated in strongly nonlinear networks [11,13,14], selective acoustic circulators [15], and topological mechanical insulators [16–18]. In nonlinear systems, the nonreciprocal behavior is a function of the nonlinear potential and may be tuned by the wave amplitude [19,20]. Recently, theoretical proposals [21–24] suggested the use of external, spatiotemporal modulation of a material's properties as a means to achieve nonreciprocity within the linear operating regime.

Here we demonstrate realization of a dynamic phononic lattice, in which the elastic properties can vary over time with spatiotemporal modulation. This time dependence leads to novel wave propagation behaviors such as nonreciprocity [21–24], which is very difficult to achieve in time-invariant systems. Though we focus on elastic waves in a magnetically coupled lattice, the concept extends to other types of waves such as thermal diodes [25] and photonic systems [26]. For instance, nonreciprocal propagation in photonic systems was observed in coupled, modulated waveguides [27], where modulation leads to irreversible mode conversion between the two waveguides. Our system behaves as a mechanical diode operating at tunable frequency ranges. Such a device may serve in acoustic circuits, like circulators, transducers, and imaging systems to rectify mechanical or acoustic energy flows [11].

Experimental realizations of modulation-induced nonreciprocity in a single phononic waveguide require (i) a dynamic lattice with controllable elastic properties, and (ii) a dynamic modulation with speed comparable to the wave propagation velocity. We meet these requirements by building a mass-spring chain of repelling magnets modulated by externally driven coils. The chain consists of 12 ring magnets ($m = 9.8$ g) free to slide on a supporting smooth cylindrical rail, as shown in Fig. 1(a). The first and last magnets are fixed to the rail (fixed boundary conditions). To dynamically modulate the chain, we introduce electrical coils around the 8 central ring magnets (masses 3 to 10). The electrical coils are positioned coaxially with the magnets and rest at the same center positions, $x_{0,n}$, as shown in Fig. 1(a). When a current flows through the electrical coils, they create local magnetic fields that couple to the ring magnets. When the ring magnets are at rest ($x_{0,n}$ position), they sit at the apex of the magnetic potential created by the coils and their coupling forces vanish. When the ring magnets displace, they experience either restoring or repelling forces from the coils, depending on the current direction. The coupling between each pair of ring magnets and coil is similar to a grounding spring. When the grounding spring stiffness is modulated spatiotemporally, time-reversal symmetry is broken leading to the formation

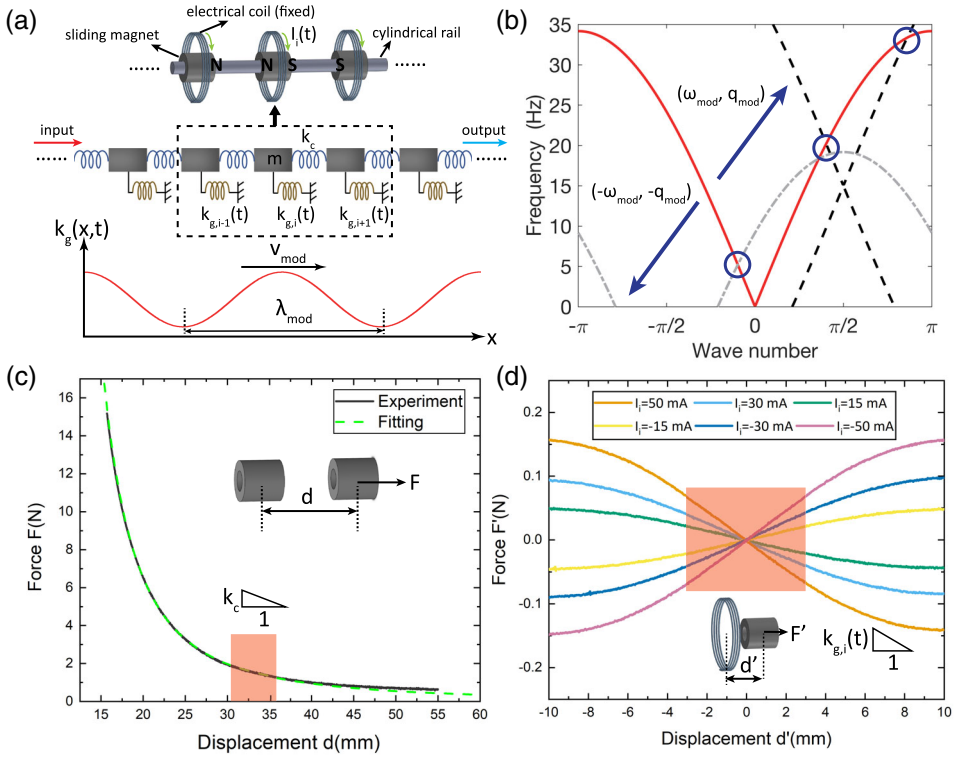

FIG. 1. Experimental setup for the nonreciprocal dynamic phononic lattice. (a) Top: Schematic of the experimental setup. Middle: Discrete mechanical representation of the system with masses and springs. Bottom: Schematic illustration of the modulation concept by changing the gounding spring stiffness (k_g) in a wavelike fashion. (b) Scattering analysis: The red solid curve describes the original dispersion relation of the unmodulated monatomic lattice. The black dashed and grey dash-dotted curves correspond to Floquet-Bloch replicas of the original curves obtained by translation along the solid blue arrows $\pm(\omega_{\mathrm{mod}}, q_{\mathrm{mod}}) = \pm(15\ \mathrm{Hz}, \pi/2)$. Parity-breaking crossings (circled) are where Bragg's condition is satisfied and nonreciprocal wave scattering is anticipated. (c) Force-displacement curve for neighboring magnetic masses, measurement (solid) and fitted curve (dashed). (d) Measured force-dispacement curves between the ring magnet and its surrounding coil at different currents. The red shaded regions in both (c) and (d) correspond to the dynamic operating regime of our experiments.

of a nonreciprocal band gap in the dispersion diagram [21–24], as shown in Fig. 1(b).

To characterize the mechanical parameters of our system, we measure the repelling force between neighboring masses as a function of their displacement (see Supplemental Material [28]). The resulting force-displacement curve exhibits a nonlinear force that is characteristic of dipole repulsion, shown in Fig. 1(c). We also measure the force between the magnets and the surrounding coils at different applied currents in Fig. 1(d). To measure the dynamic response of the system, we drive the 2nd mass with a sinusoidal force of frequency f_{dr}, and the velocity of mass 11 is monitored with a laser vibrometer (output signal). The velocity response is measured using a lock-in amplifier as a function of different f_{dr} for different modulation parameters. Because of the small vibration amplitude of the driving signal ($\lesssim$5 mm), the coupling between masses can be approximated by a linear response in the red shaded area of Fig. 1(c). The linearized coupling stiffness between adjacent magnets obtained from experiments is $k_c \approx 113$ N/m. Similarly, the coupling between the electromagnets and the masses can be linearized in the dynamic regime of interest in Fig. 1(d). We consider only the nearest neighbor interactions between masses and mass-coil pairs, since non-nearest neighbor interactions decay to a negligible amount (see Supplemental Material [28]).

The spatiotemporal modulation of the system can be achieved by applying sinusoidal alternating currents through the coils. Each coil is subjected to a current of the same frequency, f_{mod}, but with a phase shift of $\pi/2$ or $-\pi/2$ between neighbors. The equivalent grounding stiffness for the nth mass thus can be modeled as

$$k_{g,n} = k_{g,\mathrm{dc}} + k_{g,\mathrm{ac}} \cos\left(2\pi f_{\mathrm{mod}}\, t \mp \frac{\pi x_{0,n}}{2a}\right) = k_{g,\mathrm{dc}} + k_{g,\mathrm{ac}} \cos(2\pi f_{\mathrm{mod}}\, t \mp q_{\mathrm{mod}}\, n), \quad (1)$$

where $k_{g,\mathrm{dc}}$ is the small time-independent grounding stiffness added by the on-site electromagnetic force, $k_{g,\mathrm{ac}}$ is the modulation amplitude of the grounding stiffness, $x_{0,n}$ is the equilibrium position of each unit, and $q_{\mathrm{mod}} = \pm\pi/2$ is

the normalized wave number. Equation (1) describes a traveling wave with wavelength $\lambda_{\mathrm{mod}} = 4a$ and speed $v_{\mathrm{mod}} = 4af_{\mathrm{mod}}$. The modulation amplitude measured in our experiments is $k_{g,\mathrm{ac}} = 24$ N/m, which is 21% of the coupling stiffness, k_c. The constant part of the grounding stiffness is $k_{g,\mathrm{dc}} = 2.4$ N/m, which is 1 order of magnitude smaller than the oscillatory component.

In the absence of modulation ($k_{g,\mathrm{ac}} = 0$), the dispersion relation for an incident small-amplitude plane wave $u_0(n,t) = U_0 \exp[i(qn - \omega t)]$ is described by $D(\omega, q) = k_{g,\mathrm{dc}} - m\omega^2 + 4k_c \sin^2(q/2) = 0$. Modulating the lattice harmonically with $(f_{\mathrm{mod}}, q_{\mathrm{mod}})$ generates an additional scattered field $u_s(n,t) = U_s \exp[i(q_s n - \omega_s t)]$ whose mode is *shifted* by an amount $(\omega_{\mathrm{mod}}, q_{\mathrm{mod}})$ due to spatio-temporal periodicity: $(\omega_s, q_s) = (\omega_0, q_0) \pm (\omega_{\mathrm{mod}}, q_{\mathrm{mod}})$. The scattered field is negligible $(U_s \ll U_0)$ except when it is resonant with the incident field, i.e., when the modified Bragg's condition $D(\omega_s, q_s) = D(\omega_0, q_0) = 0$ is met [22]. Graphically, scattered modes are located at crossings between the original $[D(\omega, q) = 0]$ and shifted $[D(\omega_s, q_s) = 0]$ dispersion curves. Note that the crossings are nonsymmetrically distributed in a way that breaks parity of the dispersion diagram and, ultimately, reciprocity of wave propagation. Depending on whether $q_0 q_s$ is positive or negative, the scattered mode propagates either with or against the incident wave, i.e., is either transmitted or reflected. In both cases however, its frequency is shifted away from the incident frequency ω_0. This translates into a one-way dip in the transmission spectrum around ω_0.

We first set the modulation frequency to $f_{\mathrm{mod}} = 15$ Hz, which falls within the pass band of the monoatomic lattice. For this modulation frequency, three crossings exist at 5, 19, and 33 Hz and nonreciprocal wave characteristics are anticipated for neighboring driving frequencies, f_{dr}, as shown in Fig. 2(a). We measure the velocity of the second to last mass in the array as a function of the driving frequency f_{dr} in Fig. 2(b). The velocity profiles differ when the acoustic waves are traveling in the same (red) or opposite (blue) direction to the modulation wave, at driving frequencies close to $f_{\mathrm{dr}} = 19.6$ Hz. We define the codirectional or contradirectional bias ratio as $r = U^-/U^+$, where $U^{\mp}$ denotes the velocity response amplitude for $q_{\mathrm{mod}} = \mp\pi/2$. At $f_{\mathrm{dr}} = 19.6$ Hz, the measured velocity response profile in time shows that waves traveling in opposite directions have different amplitudes and profiles, with a bias of $r \approx 2.9$, shown in Figs. 2(b), 2(c). The time-domain amplitudes are lower than the amplitudes obtained from the velocity response functions. This is due to the anharmonic nature of the response in the modulated lattice. However, results demonstrate that the signal transfer around $f_{\mathrm{dr}} = 19.6$ Hz is strongly enhanced when traveling along the modulation direction and suppressed in the other direction, thus exhibiting a nonreciprocal behavior.

We developed a mathematical model to capture the dynamic characteristics of the modulated lattice. The system can be described as

$$m\ddot{u}_n + F_{\mathrm{loss}} + k_{g,n}u_n + F_{\mathrm{coupl}} = \delta_{2,n} A \cos(2\pi f_{\mathrm{dr}} t) \quad (2)$$

for $1 \le n \le 12$. Here, $u_n(t) = 0$ at the two boundaries $n = 1$, 12. $F_{\mathrm{loss}} = b\dot{u}_n + \mu \mathrm{sign}(u_n)$ represents dissipative forces within the chain, with viscous damping coefficient $b = 0.056$ kg/s and Coulomb friction coefficient $\mu = 0.012$ N (see Supplemental Material [28]). The coupling force term is $F_{\mathrm{coupl}} = P(a - u_n + u_{n+1}) - P(a - u_{n-1} + u_n)$, where we

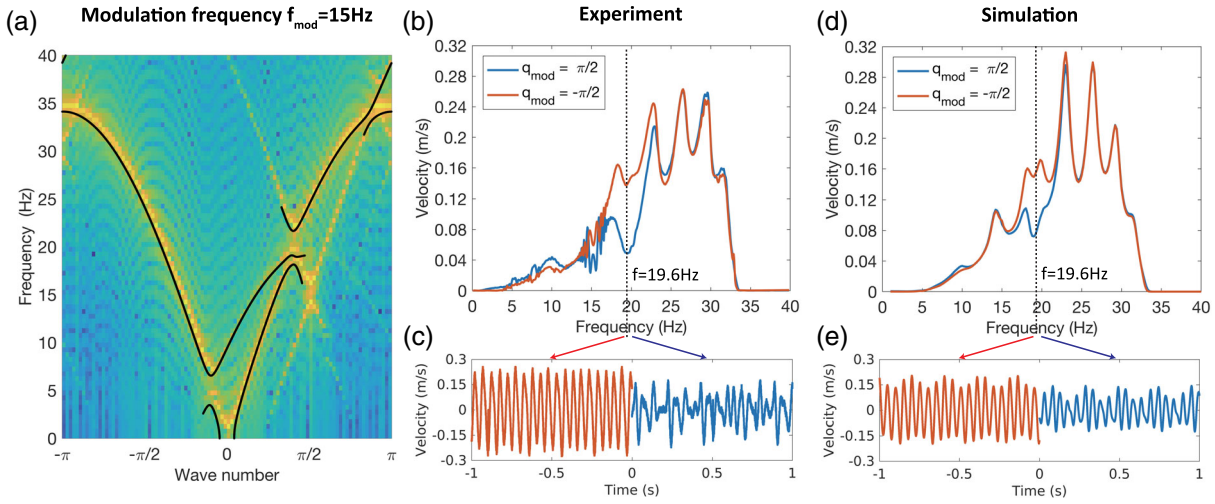

FIG. 2. Nonreciprocal wave propagation for $f_{mod} = 15$ Hz. (a) Dispersion diagram of the modulated lattice calculated by Fourier analysis of simulated velocity fields (color map) and analytically by coupled mode theory (solid black line). (b) Measured velocity response function. The amplitude ratio at 19.6 Hz is $r = 2.9$. (c) Measured velocity time series at $f_{dr} = 19.6$ Hz. The time series for $q_{\mathrm{mod}} = -\pi/2$ is shown along the negative time axis for better illustration. (d) and (e) are the simulation results corresponding to (b) and (c), respectively. The simulated amplitude ratio at 19.6 Hz is $r = 1.9$ in panel (d).

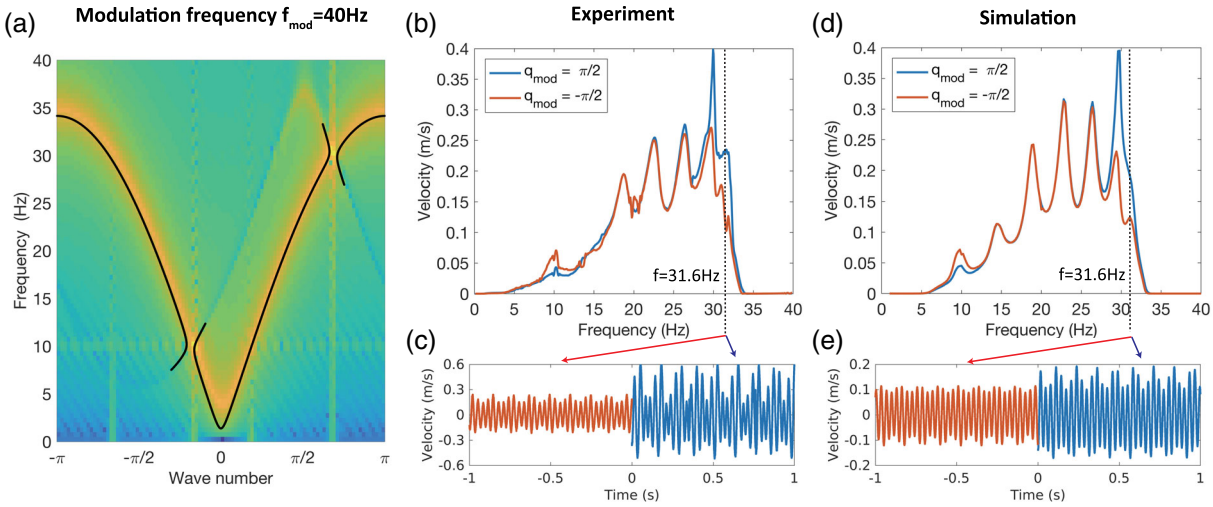

FIG. 3. Nonreciprocal wave propagation for $f_{mod} = 40$ Hz. (a) Dispersion diagram of the modulated lattice calculated by Fourier analysis of simulated velocity fields (color map) and analytically by coupled mode theory (solid black line). (b) Measured velocity response function. The amplitude ratios are $r = 1.8$ at 9.8 Hz and $r = 0.4$ at 31.6 Hz. (c) Measured velocity time series at $f_{dr} = 31.6$ Hz. The time series for $q_{\mathrm{mod}} = -\pi/2$ is shown along the negative time axis for better illustration. (d) and (e) Simulation results corresponding to (b) and (c), respectively. The simulated bias ratios are $r = 1.6$ at 9.8 Hz and $r = 0.7$ at 31.6 Hz in panel (c).

use the approximation $P(x) = c_1/(x - c_2)^2$ with $c_1 = 0.9788$ mN m^2 and $c_2 = 7.748$ mm obtained from a fitting based on Fig. 1(c). $\delta_{2,n}$ is the Kronecker delta, which is 1 for $n = 2$ and zero everywhere else. The forcing amplitude $A = 0.21$ N is obtained as a fitting parameter. At this value of the forcing amplitude, the response of the system is well approximated by the linearized equations of motion (the contribution from nonlinearity is discussed in the Supplemental Material [28]). The experimental and numerical velocity response functions for a nonmodulated lattice agree well (see Supplemental Material [28]). When the modulation is turned on, the velocity profiles obtained in experiments and simulations show a similar nonreciprocal response in Figs. 2(d) and 2(e). However, the nonreciprocal behavior at $f_{\mathrm{dr}} = 19.6$ Hz is less pronounced in simulations than in measurements ($r \approx 1.9$).

We computed dispersion curves from space-time Fourier analysis of the velocity field and compared them with the ones obtained with the plane-wave expansion method in Fig. 2(a). The observed nonreciprocal wave characteristics, at $f_{\mathrm{dr}} = 19.6$ Hz, agree well with the dispersion characteristics. The dispersion curves in Figs. 1(b) and 2(a) predict nonreciprocal behavior also near 5 and 33 Hz. However, the experimental velocities are too small at these frequencies to capture the effect. Note that the analyses (numerical and theoretical) on an infinite lossless lattice [Fig. 2(a)] predicted the same frequency range for nonreciprocal wave propagation as the experiments [Fig. 2(b)] and simulations [Fig. 2(d)] on a finite lossy lattice. The effects of energy loss and finite number of units are therefore secondary to modulation effects; see Supplemental Material [28] for discussions of finite-size and loss effects.

In order to demonstrate the tunability of the nonreciprocal frequency range in our system, we next set the modulation frequency to $f_{\mathrm{mod}} = 40$ Hz, within the band gap of the underlying monatomic lattice. Our model predicts nonreciprocal wave behavior for driving frequencies near the crossings at 10 and 30 Hz, as shown in Fig. 3(a). This is also captured in the measured velocity responses in Fig. 3(b) and time domain profiles at $f_{\mathrm{dr}} = 31.6$ Hz in Fig. 3(c). Corresponding numerical simulations in Figs. 3(d), 3(e) agree very well with the measurements.

The dispersion curve of the modulated lattice in Fig. 3(a), obtained from numerical calculations, corroborates the observed nonreciprocal characteristics for $f_{\mathrm{mod}} = 40$ Hz. The dispersion curve reveals two crossings located near 30 and 10 Hz (visible as small bright yellow regions lying on the main dispersion branches). At these points, the modulation-induced scattered field is strong enough to change the overall wave field. This is evident in the velocity response functions, as $r > 1$ near 10 Hz and $r < 1$ near 30 Hz. For other points along the main dispersion branch, the scattered wave is too weak compared to the incident field to induce any noticeable nonreciprocal effects. In contrast to the case for $f_{\mathrm{mod}} = 15$ Hz, the crossing here occurs between a positive and a negative branch of the dispersion curve ($\omega_0 \omega_s < 0$) and leads to the opening of a couple of "vertical" band gaps, as shown in Fig. 3(a). Such crossings in infinite loss-less systems are characteristic of unstable interactions caused by supersonic modulation velocities, where the velocity field is continuously amplified by drawing energy from the modulation [31,32]. However, our experimental system is intrinsically lossy and finite, and remains stable in the studied regime.

The presence of losses is known to quench instabilities [33]. In our system, this translates in the presence of a sharp peak around 30 Hz in the transmission spectrum, shown in Figs. 3(b), 3(d).

In conclusion, our results provide an experimental demonstration of modulation-induced nonreciprocity in a linear phononic lattice. The operating range of our lattice is beyond the asymptotic limits that are typically enforced in the existing theoretical work. The experimental realization of dynamically modulated nonreciprocal systems opens new opportunities for sound and vibration insulation [11,12,15], phononic logic [13,14], and energy localization and trapping [34]. In the future, the phononic waveguide developed in our work could be employed to study the nonlinear dynamics of modulated lattices, a regime that has not been explored before. The design could also be miniaturized into micro- or nanoscale electromechanical systems [35–37] with tunable frequencies as basic elements for acoustic rectifying circuits.

Y. W., B. Y., and C. D. acknowledge the support from the National Science Foundation under EFRI Grant No. 1741565. H. C., H. N., and G. H. acknowledge support from the National Science Foundation under EFRI Grant No. 1641078. B. Y. acknowledges the support from the Natural Science and Engineering Research Council of CanadaNSERC. Y. W. and C. D. designed the experiment. Y. W. performed the experiments. B. Y. performed analytical and numerical modelling of the system. H. C., H. N., and G. H. performed analytical calculations on the dispersion curves. Y. W., B. Y., H. N., G. H., and C. D. wrote the manuscript. All authors interpreted the results and reviewed the manuscript.

[*] Y. W. and B. Y. contributed equally to this work.

[1] R. Martínez-Sala, J. Sancho, J. V. Sánchez, V. Gómez, J. Llinares, and F. Meseguer, Sound attenuation by sculpture, Nature (London) **378**, 241 (1995).
[2] J. H. Page, P. Sheng, H. P. Schriemer, I. Jones, X. Jing, and D. A. Weitz, Group velocity in strongly scattering media, Science **271**, 634 (1996).
[3] J. O. Vasseur, P. A. Deymier, B. Chenni, B. Djafari-Rouhani, L. Dobrzynski, and D. Prevost, Experimental and Theoretical Evidence for the Existence of Absolute Acoustic Bad Gaps in Two-Dimensional Solid Phononic Crystals, Phys. Rev. Lett. **86**, 3012 (2001).
[4] S. Yang, J. H. Page, Z. Liu, M. L. Cowan, C. T. Chan, and P. Sheng, Focusing of Sound in a 3D Phononic Crystal, Phys. Rev. Lett. **93**, 024301 (2004).
[5] N. Fang, D. Xi, J. Xu, M. Ambati, W. Srituravanich, C. Sun, and X. Zhang, Ultrasonic metamaterials with negative modulus, Nat. Mater. **5**, 452 (2006).
[6] M. H. Lu, L. Feng, and Y. F. Chen, Phononic crystals and acoustic metamaterials, Mater. Today **12**, 34 (2009).
[7] K. H. Matlack, M. Serra-Garcia, A. Palermo, S. D. Huber, and C. Daraio, Designing perturbative metamaterials from discrete models: From Veselago lenses to topological insulators, Nat. Mater. **17**, 323 (2018).
[8] O. R. Bilal, A. Foehr, and C. Daraio, Reprogrammable phononic metasurfaces, Adv. Mater. **29**, 1700628 (2017).
[9] N. Bachelard, C. Ropp, M. Dubois, R. Zhao, Y. Wang, and X. Zhang, Emergence of an enslaved phononic bandgap in a non-equilibrium pseudo-crystal, Nat. Mater. **16**, 808 (2017).
[10] H. Lamb, On reciprocal theorems in dynamics, Proc. London Math. Soc. **s1-19**, 144 (1887).
[11] B. Liang, X. S. Guo, J. Tu, D. Zhang, and J. C. Cheng, An acoustic rectifier, Nat. Mater. **9**, 989 (2010).
[12] X. F. Li, X. Ni, L. Feng, M. H. Lu, C. He, and Y. F. Chen, Tunable Unidirectional Sound Propagation Through a Sonic-Crystal-Based Acoustic Diode, Phys. Rev. Lett. **106**, 084301 (2011).
[13] N. Boechler, G. Theocharis, and C. Daraio, Bifurcation-based acoustic switching and rectification, Nat. Mater. **10**, 665 (2011).
[14] F. Li, P. Anzel, J. Yang, P. G. Kevrekidis, and C. Daraio, Granular acoustic switches and logic elements, Nat. Commun. **5**, 5311 (2014).
[15] R. Fleury, D. L. Sounas, C. F. Sieck, M. R. Haberman, and A. Alù, Sound isolation and giant linear nonreciprocity in a compact acoustic circulator, Science **343**, 516 (2014).
[16] P. Wang, L. Lu, and K. Bertoldi, Topological Phononic Crystals with One-Way Elastic Edge Waves, Phys. Rev. Lett. **115**, 104302 (2015).
[17] M. Serra-Garcia, V. Peri, R. Süsstrunk, O. R. Bilal, T. Larsen, L. G. Villanueva, and S. D. Huber Observation of a phononoic quadrupole topological insulator, Nature (London) **555**, 342 (2018).
[18] N. P. Mitchell, L. M. Nash, D. Hexner, A. M. Turner, and W. T. M. Irvine, Amorphous topological insulators constructed from random point sets, Nat. Phys. **14**, 380 (2018).
[19] Y. Z. Wang, F. M. Li, and Y. S. Wang, Influences of active control on elastic wave propagation in a weakly nonlinear phononic crystal with a monoatomic lattice chain, Int. J. Mech. Sci. **106**, 357 (2016).
[20] Y. Z. Wang and Y. S. Wang, Active control of elastic wave propagation in nonlinear phononic crystals consisting of diatomic lattice chain, Wave Motion **78**, 1 (2018).
[21] N. Swinteck, S. Matsuo, K. Runge, J. O. Vasseur, P. Lucas, and P. A. Deymier, Bulk elastic waves with unidirectional backscattering-immune topological states in a time-dependent superlattice, J. Appl. Phys. **118**, 063103 (2015).
[22] H. Nassar, H. Chen, A. N. Norris, M. R. Haberman, and G. L. Huang, Non-reciprocal wave propagation in modulated elastic metamaterials, Proc. R. Soc. A **473**, 20170188 (2017).
[23] J. Vila, R. K. Pal, M. Ruzzene, and G. Trainiti, A Bloch-based procedure for dispersion analysis of lattices with periodic time-varying properties, J. Sound Vib. **406**, 363 (2017).
[24] F. Li, C. Chong, J. Yang, P. G. Kevrekidis, and C. Daraio, Wave transmission in time- and space-variant helicoidal phononic crystals, Phys. Rev. E **90**, 053201 (2014).
[25] D. Torrent, O. Poncelet, and J. C. Batsale, Nonreciprocal Thermal Material by Spatiotemporal Modulation, Phys. Rev. Lett. **120**, 125501 (2018).
[26] D. L. Sounas and A. Alù, Non-reciprocal photonics based on time modulation, Nat. Photonics **11**, 774 (2017).

[27] H. Lira, Z. Yu, S. Fan, and M. Lipson, Electrically Driven Nonreciprocity Induced by Interband Photonic Transition on a Silicon Chip, Phys. Rev. Lett. **109**, 033901 (2012).

[28] See Supplemental Material at http://link.aps.org/supplemental/10.1103/PhysRevLett.121.194301 for calculation of dispersion curves, contribution from nonlinearity, and energy loss effects, which includes Refs. [29,30].

[29] M. J. Frazier and M. I. Hussein, Band structure of phononic crystals with general damping, J. Appl. Phys. **108**, 093506 (2010).

[30] D. J. Mead, Wave propagation and natural modes in periodic systems: I. Mono-coupled systems, J. Sound Vib. **40**, 1 (1975).

[31] H. Nassar, H. Chen, A. N. Norris, and G. L. Huang, Non-reciprocal flexural wave propagation in a modulated meta-beam, Extreme Mech. Lett. **15**, 97 (2017).

[32] H. Nassar, X. C. Xu, A. N. Norris, and G. L. Huang, Modulated phononic crystals: Non-reciprocal wave propagation and Willis materials, J. Mech. Phys. Solids **101**, 10 (2017).

[33] A. H. Nayfeh and D. T. Mook, *Nonlinear Oscillations* (John Wiley & Sons, New York, 1979).

[34] K. L. Tsakmakidis, L. Shen, S. A. Schulz, X. Zheng, J. Upham, X. Deng, H. Altug, A. F. Vakakis, and R. W. Boyd, Breaking Lorentz reciprocity to overcome the time-bandwidth limit in physics and engineering, Science **356**, 1260 (2017).

[35] X. L. Feng, C. J. White, A. Hajimiri, and M. L. Roukes, A self-sustaining ultrahigh-frequency nanoelectromechanical oscillator, Nat. Nanotechnol. **3**, 342 (2008).

[36] A. M. van der Zande, R. A. Barton, J. S. Alden, C. S. Ruiz-Vargas, W. S. Whitney, P. H. Q. Pham, J. Park, J. M. Parpia, H. G. Craighead, and P. L. McEuen, Large-scale arrays of single-layer graphene resonators, Nano Lett. **10**, 4869 (2010).

[37] J. Cha and C. Daraio, Electrical tuning of elastic wave propagation in nanomechanical lattices at MHz frequencies, Nat. Nanotechnol., doi: 10.1038/s41565-018-0252-6 (2018).